An intrinsically disordered pathological prion variant Y145Stop converts into self-seeding amyloids via liquid–liquid phase separation

Aishwarya Agarwal[a,b,1], Sandeep K. Rai[a,c,1], Anamika Avni[a,c], and Samrat Mukhopadhyay[a,b,c,2]

[a]Centre for Protein Science, Design and Engineering, Indian Institute of Science Education and Research Mohali, Punjab 140306, India; [b]Department of Biological Sciences, Indian Institute of Science Education and Research Mohali 140306 Punjab, India; and [c]Department of Chemical Sciences, Indian Institute of Science Education and Research Mohali 140306 Punjab, India

Edited by Michael K. Rosen, The University of Texas Southwestern Medical Center, Dallas, TX, and approved October 5, 2021 (received for review January 20, 2021)

Biomolecular condensation via liquid–liquid phase separation of intrinsically disordered proteins/regions (IDPs/IDRs) along with other biomolecules is proposed to control critical cellular functions, whereas aberrant phase transitions are associated with a range of neurodegenerative diseases. Here, we show that a disease-associated stop codon mutation of the prion protein (PrP) at tyrosine 145 (Y145Stop), resulting in a truncated, highly disordered, N-terminal IDR, spontaneously phase-separates into dynamic liquid-like droplets. Phase separation of this highly positively charged N-terminal segment is promoted by the electrostatic screening and a multitude of weak, transient, multivalent, intermolecular interactions. Single-droplet Raman measurements, in conjunction with an array of bioinformatic, spectroscopic, microscopic, and mutagenesis studies, revealed a highly mobile internal organization within the liquid-like condensates. The phase behavior of Y145Stop is modulated by RNA. Lower RNA:protein ratios promote condensation at a low micromolar protein concentration under physiological conditions. At higher concentrations of RNA, phase separation is abolished. Upon aging, these highly dynamic liquid-like droplets gradually transform into ordered, β-rich, amyloid-like aggregates. These aggregates formed via phase transitions display an autocatalytic self-templating characteristic involving the recruitment and binding-induced conformational conversion of monomeric Y145Stop into amyloid fibrils. In contrast to this intrinsically disordered truncated variant, the wild-type full-length PrP exhibits a much lower propensity for both condensation and maturation into amyloids, hinting at a possible protective role of the C-terminal domain. Such an interplay of molecular factors in modulating the protein phase behavior might have much broader implications in cell physiology and disease.

amyloid formation | biological phase transitions | intrinsically disordered proteins | membraneless organelles | stop codon mutation

An emerging body of research has revealed that in addition to canonical membrane-enclosed organelles, eukaryotic cells also contain organelles without delimiting membranes. These membraneless organelles, also known as biomolecular condensates, are formed via liquid–liquid phase separation (LLPS) of proteins, nucleic acids, and other biomolecules (1–11). These mesoscopic intracellular assemblies are dynamic, liquid-like, permeable, nonstoichiometric supramolecular assemblies that allow rapid exchange of components within the environment and offer unique spatiotemporal control of the macromolecular organization and cellular biochemistry. Intracellular phase transitions are governed by an intricate balance between the enthalpy and entropy of mixing and are primarily driven by intrinsically disordered proteins/regions (IDPs/IDRs) containing prion-like domains, low-complexity regions, and oligopeptide repeat domains (12–19). These domains can promote weak, dynamic, promiscuous, multivalent intermolecular contacts involving electrostatic, hydrophobic, hydrogen bonding, dipole–dipole, π–π, and cation–π interactions. The intrinsic disorder of these polypeptide chains can dynamically control the making and breaking of noncovalent interactions, giving rise to a liquid-like behavior of phase-separated biomolecular condensates. While liquid-like intracellular bodies are linked with a diverse array of cellular functions, liquid-to-gel and liquid-to-solid phase transitions are implicated in a range of debilitating neurodegenerative diseases (20–24). Therefore, there is an emerging consensus on the central role of biomolecular condensation and maturation promoting more persistent intermolecular contacts in aberrant pathological phase transitions.

The conformational conversion of the human prion protein (PrP) into a misfolded, β-rich, aggregated, self-replicating amyloid-like form is associated with a range of invariably fatal and transmissible neurodegenerative diseases classified under transmissible spongiform encephalopathies (25, 26). This class of diseases is either caused by a spontaneous prion misfolding leading to sporadic Creutzfeldt–Jakob disease (CJD) or due to mutations in the *prnp* gene resulting in familial CJD, fatal familial insomnia (FFI), and Gerstmann-Sträussler-Scheinker (GSS) syndrome

Significance

Biology has evolved to achieve precise spatiotemporal control of crucial cellular functions through liquid–liquid phase separation of highly flexible proteins and nucleic acids into membraneless organelles. However, these liquid-like intracellular condensates can undergo irreversible phase transitions into solid-like aggregates associated with deadly human diseases. Here, we show that a pathological truncation variant of the prion protein comprising the N-terminal unstructured domain spontaneously phase-separates into liquid droplets under physiological conditions. These liquid-like condensates gradually mature into solid-like self-replicable amyloids reminiscent of toxic misfolded proteinaceous aggregates involved in transmissible prion diseases. This aberrant phase-transition propensity is suppressed in the full-length protein, which may indicate an evolutionarily conserved role of an intriguing relationship between different domains in modulating the protein phase behavior.

Author contributions: A. Agarwal and S.M. designed research; A. Agarwal, S.K.R., and A. Avni performed research; A. Agarwal contributed new reagents/analytic tools; A. Agarwal, S.K.R., and A. Avni analyzed data; and A. Agarwal, S.K.R., A. Avni, and S.M. wrote the paper.

The authors declare no competing interest.

This article is a PNAS Direct Submission.

[1]A. Agarwal and S.K.R. contributed equally to this work.

[2]To whom correspondence may be addressed. Email: mukhopadhyay@iisermohali.ac.in.

This article contains supporting information online at http://www.pnas.org/lookup/suppl/doi:10.1073/pnas.2100968118/-/DCSupplemental.

Published November 5, 2021.

(25–27). Cellular PrP is a glycosylphosphatidylinositol-anchored (GPI-anchored), 253-residue, cell-surface protein consisting of an N-terminal signal peptide (residues 1 to 23) that is cleaved upon maturation, a positively charged unstructured N-terminal tail (residues 23 to 120), a structured C-terminal domain (residues 121 to 230), and a GPI-anchor signal (residues 231 to 253) (Fig. 1 *A* and *B*) (25–28). The N-terminal unstructured domain can be classified as an IDR that comprises two lysine clusters

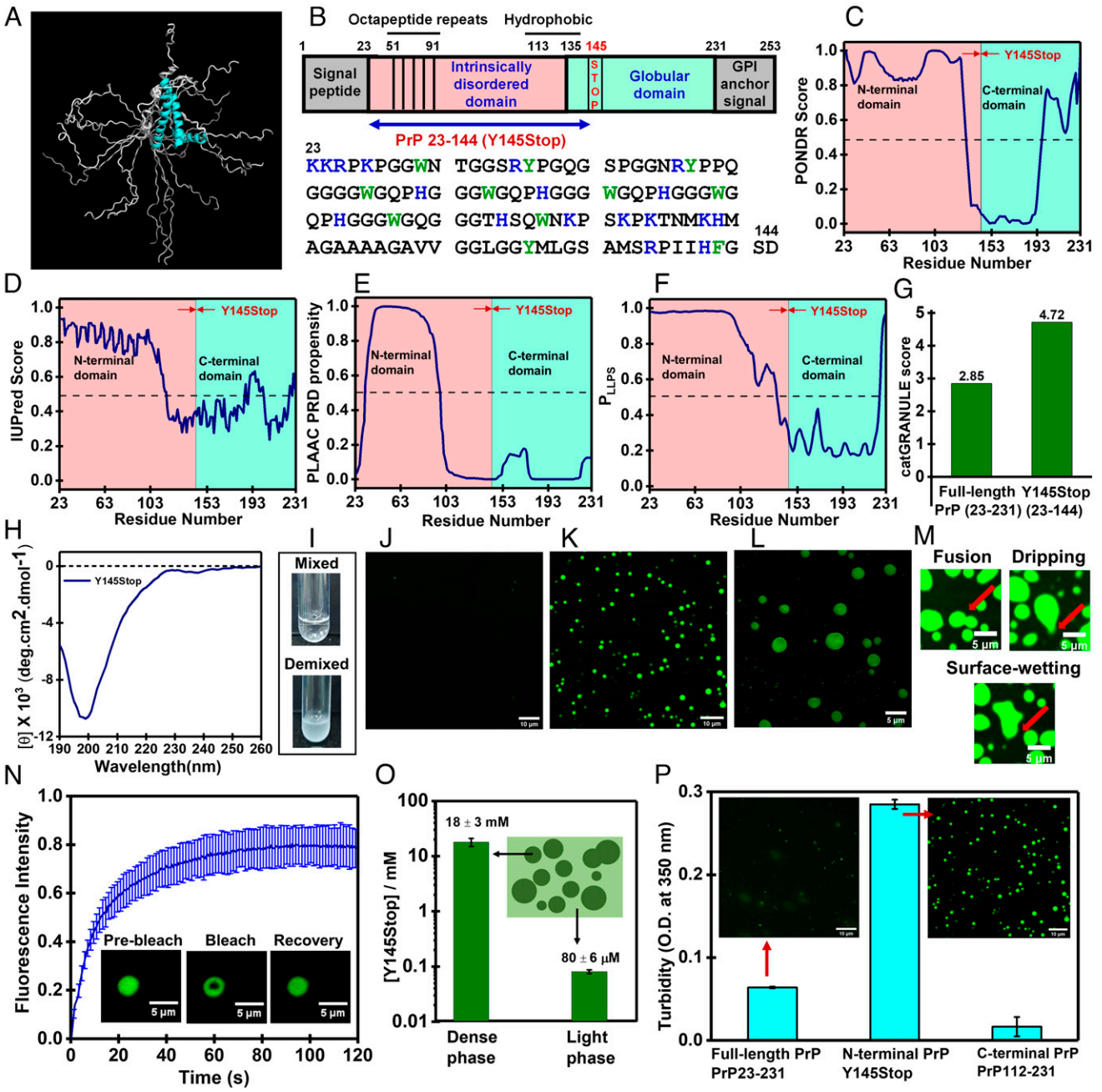

Fig. 1. Phase separation of PrP-Y145Stop. (*A*) Overlay of 20 conformations obtained from the NMR structure of human PrP90-231 (PDB ID code 2LSB) (28) generated using PyMOL (Schrödinger) showing conformational heterogeneity at the N-terminal domain. (*B*) Schematic representation of PrP indicating all the segments and domains (Y145Stop is also highlighted). The amino acid sequence of Y145Stop (residues 23 to 144) showing positively charged residues (blue) and aromatic residues (green). The disorder prediction tools PONDR (37) (*C*) and IUPred (38) (*D*) indicate a highly unstructured N-terminal segment of PrP. A boundary between disordered and ordered regions is shown at residues 145 (this boundary is conventionally shown at residue 121). (*E*) The presence of a yeast prion-like domain from residues 32 to 97 using PLAAC (39). Prediction of LLPS propensity using FuzDrop (4) (*F*) and catGRANULE (41) (*G*). The FuzDrop LLPS probability (P_{LLPS}) for the N-terminal IDR (Y145Stop) is 0.997 and for the C-terminal fragment (PrP 112 to 231) is 0.250. (*H*) A CD spectrum of Y145Stop showing a random-coil conformation. (*I*) Spontaneous LLPS of Y145Stop (100 µM, pH 7.5, 37 °C) from a homogeneous mixed-phase into a demixed phase upon the addition of salt (350 mM NaCl). Confocal images of homogeneous phase (*J*) and droplets (*K*) performed using fluorescein-labeled Y145Stop single-Cys mutant at residue 31. (*L*) Lattice structured illumination microscopy images of droplets using Alexa488-labeled protein. (*M*) Droplet fusions, dripping, and surface-wetting using confocal microscopy. See Movie S1 for a video of droplet fusions. (*N*) FRAP kinetics of multiple droplets (1% Alexa488-labeled protein; $n = 10$) (*SI Appendix, Methods*). (*O*) Dense phase and dilute phase concentrations of Y145Stop droplets estimated using centrifugation (42) (mean ± SEM; $n = 4$). The protein concentration is plotted in the log scale to clearly show high and low concentrations for dense and light phases, respectively. (*P*) Comparison of phase separation ability of Y145Stop, full-length PrP, and the C-terminal segment using turbidity and confocal microscopy imaging. For Y145Stop, the image shown in *K* is included here for comparison.

(residues 23 to 30 and 100 to 110), five glycine-rich octapeptide repeats (PHGGGWGQ), and a hydrophobic segment (residues 113 to 135).

In contrast, the C-terminal domain is highly structured and consists of three α-helices (residues 144 to 154, 175 to 193, and 200 to 219) and two short antiparallel β-strands (128 to 131 and 161 to 164) (Fig. 1*B*). In vitro prion conversions and amplifications from recombinantly expressed PrP recapitulate several key structural and biochemical characteristics of pathogenic prion deposits (29–31). An unusual pathological mutation of the tyrosine at residue 145 to a stop codon (PrP-Y145Stop) results in an intracellular, C-terminally truncated, and a highly unstructured variant of the protein that exhibits the GSS-like phenotype and familial cerebral amyloid angiopathy (CAA) (32–34). Under normal conditions, this fragment is unstable and is rapidly degraded in the cell; however, under stress conditions, Y145Stop accumulates in the endoplasmic reticulum, Golgi, and nucleus. This truncation mutation results in pathological amyloid deposits in the brain (35, 36). In this work, we show that intrinsically disordered Y145Stop spontaneously phase-separates into highly dynamic liquid-like droplets that undergo a time-dependent maturation into ordered, solid-like, self-templating amyloid aggregates via a liquid-to-solid phase transition. The prion phase behavior can be modulated by RNA that tunes the material property of these condensates. The LLPS-mediated conformational switch of Y145Stop provides a mechanistic underpinning of effective nucleation and transition into self-replicating pernicious amyloid-like species.

Results

PrP Y145Stop Undergoes LLPS In Vitro. In order to examine the presence of intrinsic disorder in human Y145Stop, we first used well-known bioinformatic prediction tools (37–39) (Fig. 1 *B*–*G*). These studies revealed a domain (residues 32 to 97) predicted to be highly disordered, enriched in polar residues, thus termed "prion-like" for its resemblance in sequence composition to yeast prions (39). The disordered state was further confirmed by monitoring circular dichroism (CD) of recombinantly expressed human PrP Y145Stop (Fig. 1*H*). We next used a sequence-based prediction of fuzzy protein interactions (40) to predict the droplet formation propensity of Y145Stop. The phase separation prediction tools, such as FuzDrop (4) and catGRANULE (41), revealed a high LLPS propensity of intrinsically disordered Y145Stop (Fig. 1 *F* and *G*). To experimentally verify the LLPS phenomenon of PrP Y145Stop, we began by characterizing its phase behavior in vitro using turbidity measurements and fluorescence microscopy. Under the cytosolic condition (pH 7.5, 37 °C), Y145Stop even at a high protein concentration (100 μM) remained clear and dispersed. Upon addition of increasing amounts of salt, the turbidity of the protein solution rose, immediately indicating phase separation at a cytosolic pH (Fig. 1*I*).

We next created a single-Cys mutant at residue position 31 of Y145Stop to be able to label the protein using thiol-active fluorescent dyes, such as fluorescein-5-maleimide, Alexa Fluor488 maleimide, and Alexa Fluor594 maleimide. Y145Stop mixed with fluorescently labeled protein (1%) was used for confocal and structured illumination microscopy imaging of droplets (Fig. 1 *J*–*L*). These fluorescent droplets undergo fusion, surface-wetting, dripping, and exhibit fast fluorescence recovery after photobleaching (FRAP), highlighting their liquid-like nature (Fig. 1 *M* and *N*). The concentration of the dense phase was determined using the centrifugation method that allows an accurate estimation of the protein concentration in the dense phase (42). The dense-phase concentration was found to be ∼20 mM (∼250 mg/mL), which is ∼250 times denser compared to the light phase (∼80 μM) that corresponds to the critical saturation concentration, C_{sat} (Fig. 1*O*). A similar dense-phase concentration was reported for an IDR of Ddx4 (43) and the FUS low-complexity domain (44). Next, we performed fluorescence anisotropy measurements that revealed no significant hindrance in the rotational relaxation of the polypeptide chain upon LLPS, indicating a mobile interior within the droplets (*SI Appendix*, Fig. S1*A*). To mimic the cellular environment, we also studied phase separation of Y145Stop in the presence of a molecular crowding agent, such as polyethylene glycol (PEG). In the presence of 10% PEG, Y145Stop undergoes LLPS at a much lower protein concentration and a physiological salt concentration (150 mM) (*SI Appendix*, Fig. S1*B*).

Taken together, these results demonstrate that the N-terminal IDR of PrP, Y145Stop, under the near-physiological condition, undergoes condensation into liquid-like droplets with a protein-rich, dense, yet highly mobile environment within the droplets. The predicted net charge of this domain is +10.4 at pH 7.5, and therefore, intermolecular repulsions between highly charged polypeptide chains prevent phase separation at low ionic strength. At higher salt concentrations, due to the effective charge-screening, polypeptide chains can commingle via weak, noncovalent, interchain interactions facilitating LLPS of this N-terminal IDR devoid of the C-terminal globular domain. Next, we asked what the role of the C-terminal globular domain in modulating the prion phase behavior is. PrP comprising both N- and C-terminal domains undergoes phase separation (45–47). However, under our condition, the phase separation propensity of the full-length PrP (PrP 23 to 231) was much lower than the N-terminal IDR, Y145Stop (Fig. 1*P*). This observation is consistent with the predictions (Fig. 1 *F* and *G*).

In order to further investigate the role of the C-terminal folded domain, we created an N-terminally truncated variant (PrP 112 to 231), which contains the entire C-terminal globular domain and a much shorter N-terminal tail. As expected, this construct is well-folded into a helical structure, as evident by CD (*SI Appendix*, Fig. S1*C*). PrP 112 to 231 did not phase-separate even after prolonged incubation under our conditions in the presence or absence of salt. Therefore, our experimental observations corroborate the results obtained from the prediction tools and suggest that the C-terminal globular domain alone is not prone to LLPS. In fact, the presence of this globular domain in full-length PrP diminishes the overall LLPS propensity considerably, as indicated by prediction tools and experiments (Fig. 1 *F*, *G*, and *P*). Together, these observations indicated that the N-terminal IDR (Y145Stop) is the principal driver of PrP phase separation, consistent with a recent study (47), whereas the presence of the C-terminal domain might potentially lower the LLPS propensity.

The Role of RNA in Modulating the Phase Behavior of Y145Stop. Nucleic acids have been shown to be associated with PrP and to act as the cofactor of PrP (36, 48–51). Furthermore, the formation of ribonucleoprotein granules by cytoplasmic PrP has been observed (51). The N-terminal IDR involving the Y145Stop fragment has been broadly classified under the umbrella of RNA-binding proteins due to the presence of two highly conserved polybasic regions containing lysine clusters that have charge complementarity to nucleic acids (36, 49). Therefore, it is imperative to elucidate the role of RNA in modulating the phase behavior of Y145Stop. The addition of crude tRNA as low as 100 ng resulted in phase separation, as confirmed using turbidity assays and confocal microscopy. The presence of RNA drastically lowered the saturation concentration of the protein to as low as 5 μM in the presence of 150 mM NaCl (Fig. 2 *A* and *B*). These droplets were initially spherical and rapidly transformed into nonspherical condensates lacking the ability to fuse. In order to test whether these were gel-like, less

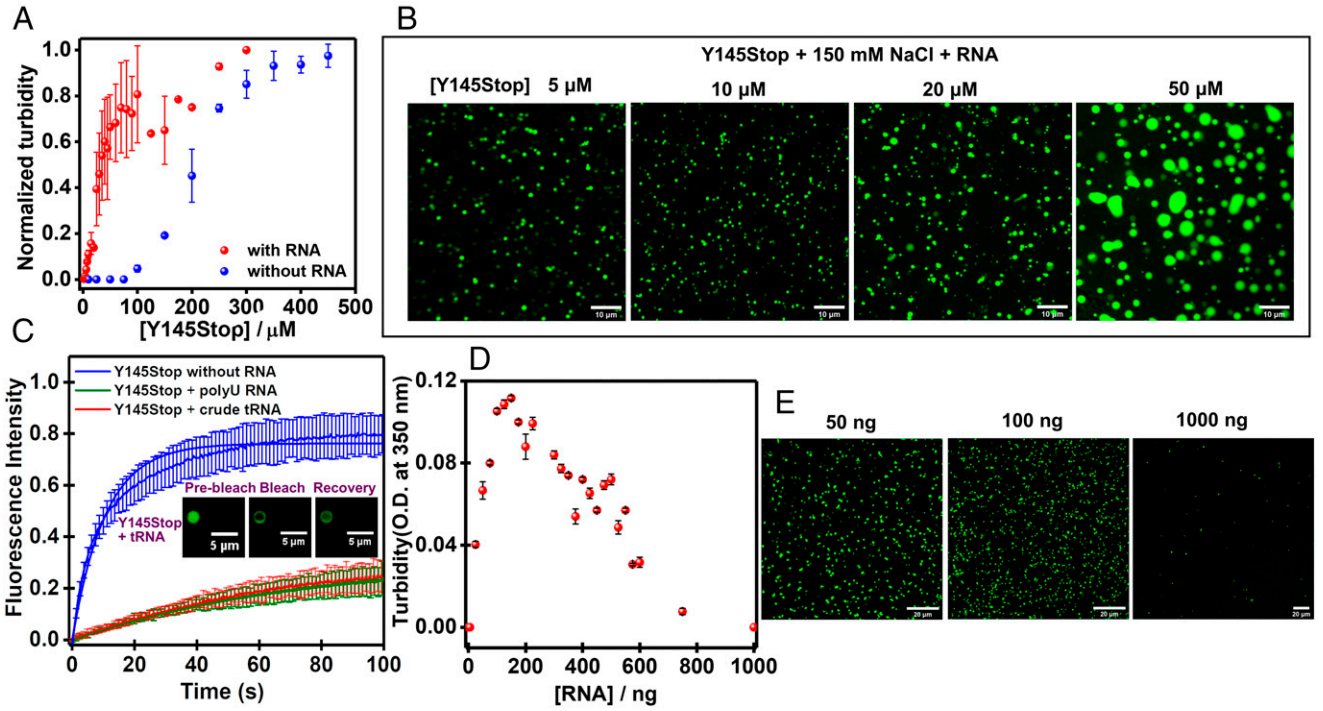

Fig. 2. Modulation of Y145Stop phase transitions by RNA. RNA lowers the Y145Stop concentration required for phase separation from ~80 μM to ~5 μM of protein at 150 mM NaCl and pH 7.5 as observed by the turbidity assay (*A*) and confocal microscopy (*B*) using crude tRNA. (*C*) FRAP kinetics of multiple Y145Stop droplets (1% Alexa488-labeled Y145Stop, $n = 8$) in the absence and the presence of RNA (crude tRNA and polyU RNA). The solid lines represent the fitted curves (*SI Appendix, Methods*). The fluorescence images of droplets during FRAP measurements are also shown. (*D* and *E*) Low RNA/protein ratios promote phase separation and high ratios inhibit phase separation at a fixed (10 μM) Y145Stop concentration as observed by the RNA concentration-dependent turbidity assays and confocal microscopy (polyU RNA).

dynamic condensates, we next performed FRAP experiments and quantified the protein diffusivity within these RNA-protein condensates. We observed much slower and incomplete recovery of these RNA-induced droplets (~20%) as compared to salt-induced droplets (~80%), indicating a hardening of the material property of RNA-Y145Stop condensates (Fig. 2*C*). In order to rule out the possibility of specificity of RNA in the observed phase behavior of Y145Stop, we also performed phase separation assays in the presence of other RNAs, such as polyU RNA and yeast total RNA. Our results showed a similar ability of these RNAs in modulating the phase behavior of Y145Stop (*SI Appendix*, Fig. S2).

Next, to establish if the RNA-induced LLPS resulted in a more viscous gel-like interior, we recovered the apparent diffusion coefficients of the protein within the droplets (*SI Appendix*, *Methods*). In the absence of RNA, the FRAP recovery was on a faster timescale, with a $t_{1/2}$ of 7.3 s that yielded an approximate diffusion coefficient of ~0.034 $\mu m^2\ s^{-1}$. The recovery kinetics in the presence of RNA was much slower ($t_{1/2}$ = 34.5 s), indicating a considerable drop in the apparent diffusion coefficient (~0.007 $\mu m^2\ s^{-1}$). Therefore, the RNA-induced droplets are associated with lower protein diffusivity and enhanced internal viscosity. Next, we studied the effect of the RNA concentration on the phase separation of Y145Stop. We found that the phase separation ability of the protein is highly enhanced at a low RNA concentration, whereas at higher concentrations of RNA, no phase separation was observed (Fig. 2 *D* and *E*). Protein solutions with high RNA concentrations remained dispersed and perfectly mixed even upon longer incubation. The interaction of polyanions, such as RNAs with the positively charged N-terminal domain, possibly results in the charge inversion that prevents phase separation. Such an RNA stoichiometry-dependent promotion and inhibition of phase transition has been previously observed for others IDPs and prion-like domains (52–58). Together, these results suggest that RNA buffers the phase behavior of Y145Stop and tunes the material property of the condensates.

Conformational Heterogeneity and Disorder within the Droplets Captured by Vibrational Raman Spectroscopy. Next, we set out to discern the key structural characteristics of polypeptide chains within Y145Stop liquid droplets. In order to elucidate the protein conformational states, we employed vibrational Raman spectroscopy that provides a wealth of molecular information about the polypeptide backbones and sidechains (59, 60). Additionally, a laser Raman set-up equipped with a microscope allows us to focus the laser beam into the protein-rich, dense, condensed phase of individual droplets to capture Raman scattering bands associated with a multitude of molecular vibrational modes from protein-rich single droplets. The Raman spectra of dispersed and phase-separated states of Y145Stop clearly showed characteristic bands corresponding to backbone amide I, amide III, Trp, Tyr, Phe, and other vibrational modes (Fig. 3*A*). Amide I (1,630 to 1,700 cm^{-1}) originates primarily due to the C = O stretching of the polypeptide backbone, whereas amide III (1,230 to 1,300 cm^{-1}) corresponds to a combination of N-H bending and C-N stretching modes (59, 60). These amide vibrational bands are often used to identify the secondary structural elements in proteins. Broad amide I bands for both dispersed and demixed phases exhibited highly disordered conformations. A closer inspection of amide I revealed an increase in the full-width at half maximum (FWHM) from the dispersed phase (~55 cm^{-1}) to the droplet phase (~63 cm^{-1}), indicating a higher conformational heterogeneity in the condensed phase (Fig. 3*B*).

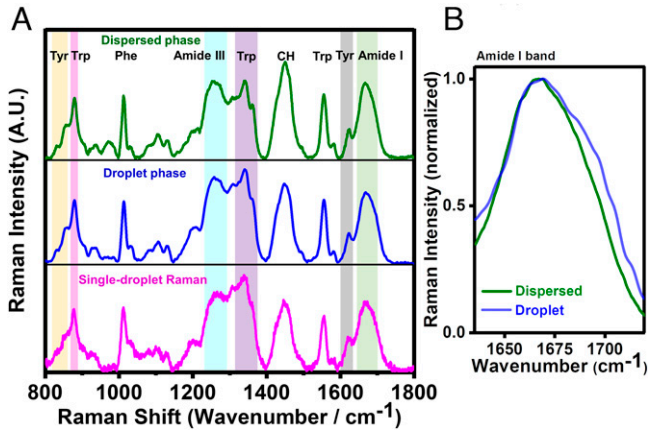

Fig. 3. Vibrational Raman spectroscopy of Y145Stop. (*A*) Bulk Raman spectra of dispersed (olive) and droplet phases (blue) and single-droplet Raman (magenta). Prominent vibrational signatures of amide backbones and sidechains are shaded and labeled. (*B*) The amide I regions are shown for dispersed and droplet phases.

Next, we determined the intensity ratio of the tyrosine Fermi doublet (I_{850}/I_{830}) that serves as an indicator of the hydrogen bonding strength between the phenolic hydroxyl group of Tyr and the neighboring water molecules in the vicinity. This ratio was ~2.7 for both dispersed and droplets indicating little or no changes in the solvent accessibility of polypeptide chains in the liquid-like condensed phase (*SI Appendix*, Fig. S3). The intensity ratio for the tryptophan Fermi doublet (I_{1360}/I_{1340}) (hydrophobicity) and a band at 880 cm^{-1} (hydrogen bonding strength between water and N-H of the indole ring) did not exhibit any measurable changes upon the liquid phase condensation. We were able to recapitulate all these vibrational signatures in our single-droplet Raman studies. Taken together, these results demonstrate that Y145Stop retains its intrinsic disorder with a slight increase in the structural heterogeneity within the demixed liquid droplets. Next, we aimed at delineating the interplay of noncovalent interactions responsible for Y145Stop phase separation.

Intermolecular Interactions Driving Phase Separation of Y145Stop.

Electrostatic screening. Y145Stop carries a high net positive charge (~+10.4) at pH 7.5. Interchain repulsions prohibit intermolecular interactions that are essential for LLPS. In order to screen the high positive charge and to allow an effective interchain association, a threshold salt concentration is required above which it should phase-separate via homotypic multivalent interactions. To unveil the role of electrostatic screening, we constructed the phase diagram as a function of salt concentration. Y145Stop phase-separates above a critical threshold salt concentration (> 300 mM, pH 7.5) and remains phase-separated throughout the entire NaCl concentration range (Fig. 4 *A* and *B* and *SI Appendix*, Fig. S4*A*). At a high salt concentration (750 mM NaCl), phase separation was observed at a much lower protein concentration (Fig. 4*B*). To further support the role of electrostatic screening, we altered the charge-state of the protein by varying the solution pH at a fixed salt concentration. Both turbidity measurements and confocal imaging at different pH (pH 5.8, 7.5, and 8.8) at a fixed ionic strength showed an enhanced phase separation with an increase in the pH (*SI Appendix*, Fig. S4 *B* and *C*). The protein at a mildly acidic pH (pH 5.8) carries a higher net positive charge (~+15), and therefore requires a greater screening effect for phase separation compared to the protein at a mildly alkaline pH (pH 8.8) containing a lower net positive charge (~+8.5). These observations indicated that electrostatic screening is critical for phase separation of Y145Stop. An increase in the salt concentration decreases the Debye length, allowing the screening of electrostatic repulsions between the positively charged residues, resulting in the phase transition (61). Since at higher salt concentrations the electrostatic interactions are negligible but the hydrophobic effect may be important, we next set out to characterize the role of hydrophobic interactions in driving phase separation of Y145Stop.

Hydrophobic interactions. In order to characterize the role of hydrophobic interactions in promoting phase separation, we first used 1,6-hexanediol, an aliphatic alcohol, that has been proposed to disrupt weak hydrophobic interactions although the exact mechanism is not clear (62). Phase separation was inhibited by 2% (wt/vol) 1,6-hexanediol, indicating an important role of weak hydrophobic interactions in LLPS of Y145Stop (Fig. 4*C* and *SI Appendix*, Fig. S5*A*). We also used 8-anilino-1-naphthalenesulfonic acid (ANS), which is a well-known hydrophobic reporter. We observed a blue shift and an increase in the ANS fluorescence intensity upon LLPS of Y145Stop, indicating the presence of local hydrophobic patches within the droplets (*SI Appendix*, Fig. S5*B*). However, we would like to point out that the interpretation of the ANS fluorescence characteristics in the condensed phase may not be straightforward. A closer look at the amino acid sequence of Y145Stop revealed the presence of a hydrophobic stretch that is rich in alanine and valine residues (Fig. 1*B*). We further evaluated the role of hydrophobicity by performing site-directed mutagenesis at the hydrophobic stretch. We mutated residues by substituting three alanines-to-valines (A→V) to increase the hydrophobicity and alanines-to-glycines (A→G) to decrease the hydrophobicity. These mutations did not alter the structural attributes of Y145Stop as verified using CD measurements (*SI Appendix*, Fig. S5*C*). Glycine is polar, structurally flexible, and does not appear to alter the saturation concentration (63). As expected, the substitution of alanines-to-glycines (Y145StopA→G) afforded droplets with a bit enhanced fluidity and behaved similarly to the wild-type Y145Stop (Fig. 4 *D*–*F*). However, the mutations of alanines-to-valines (Y145StopA→V) considerably enhanced the LLPS propensity (Fig. 4*D*) and resulted in more gel-like/solid-like droplets, as revealed by irregular shape in confocal microscopy associated with much lower FRAP recovery (Fig. 4 *E* and *F*).

We also performed FRAP experiments for Y145Stop and Y145StopA→V at different salt concentrations to arrive at equivalent points in the phase diagram where the protein concentration in the dense phase was similar for both the constructs (*SI Appendix*, Fig. S5*D*). Similar recovery kinetics revealed that the observed change in the material property was primarily due to the phase diagram shift upon A→V mutation (*SI Appendix*, Fig. S5*E*). Together, these results show that the mutations in the hydrophobic segment alter the phase behavior, highlighting the role of hydrophobicity in driving the phase separation of Y145Stop. If the hydrophobic effect is a primary molecular driver of the phase transition, we would expect to observe higher phase separation propensity at higher temperatures due to the increase in the entropic contributions. Therefore, our next goal was to examine the thermo-responsive phase behavior of Y145Stop.

Thermo-responsive phase behavior. Based on the amino acid composition, IDPs exhibit the upper critical solution transition (UCST) and the lower critical solution transition (LCST) (16, 64). Polar sequences interspersed by aromatic and charged residues display the UCST behavior, whereas hydrophobic/aromatic-rich sequences follow the LCST behavior since the hydrophobic effect being largely entropic is more pronounced at a higher temperature. In order to characterize the temperature-dependent phase transition of Y145Stop, we performed the turbidity assay as a function of temperature, ranging

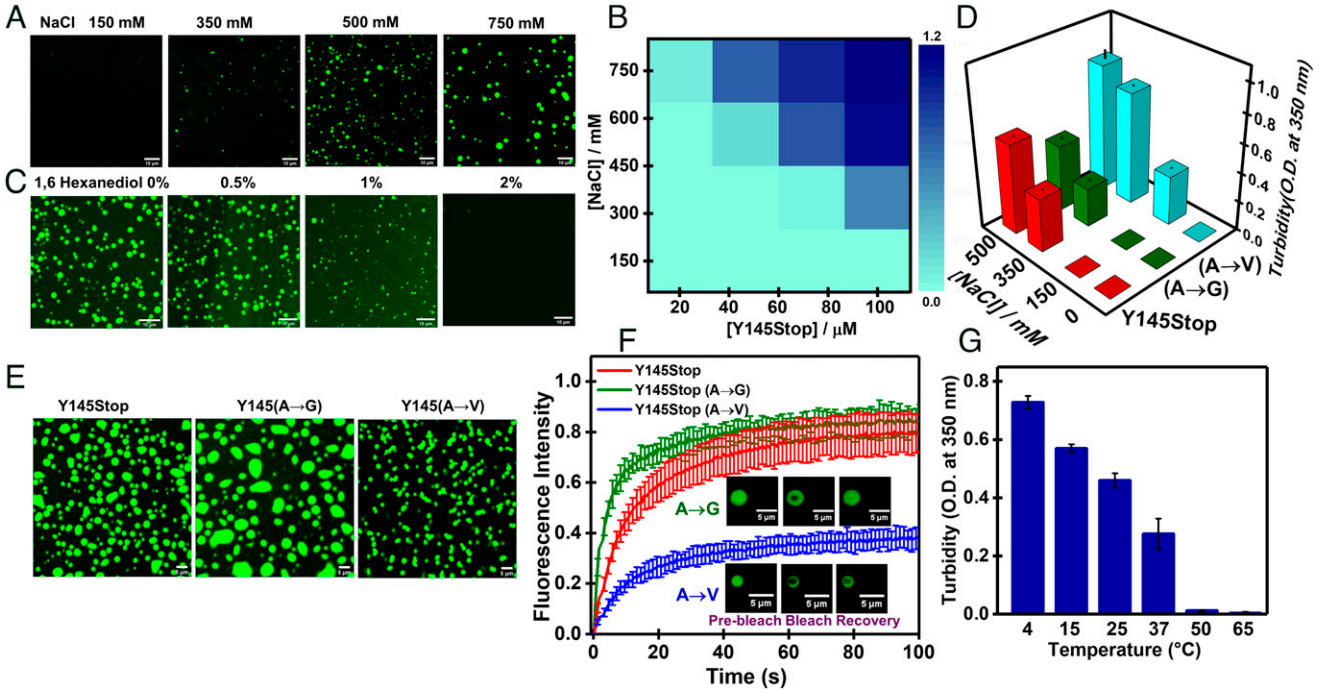

Fig. 4. Molecular determinants of phase separation. (*A*) Confocal images of fluorescently labeled Y145Stop (100 μM, pH 7.5, 37 °C) as a function of increasing NaCl concentrations. (*B*) A phase diagram at different protein and salt concentrations constructed from mean turbidity values. (*C*) Confocal images of droplets in the presence of increasing amounts of 1,6-hexanediol (100 μM Y145Stop, 350 mM NaCl, pH 7.5, 37 °C). (*D*) Turbidity plot for Y145Stop, and variants A→G and A→V (at residues 113, 115, and 117) in the presence of different concentrations of salt. (*E*) Confocal images of Y145Stop and variants A→G and A→V (100 μM protein, 350 mM NaCl, pH 7.5, 37 °C) (*F*) FRAP kinetics of multiple fluorescently labeled droplets of Y145Stop and variants A→G and A→V (mean ± SEM; $n = 8$). FRAP kinetics at equivalent points having a similar dense-phase concentration are shown in *SI Appendix*, Fig. S5*E*. (*G*) Phase separation of Y145Stop as a function of temperature.

from 4 °C to 65 °C. Interestingly, we observed an increase in the phase separation at lower temperatures indicating a UCST behavior (Fig. 4*G*), as previously observed for other prion-like domains. These droplets exhibited temperature-dependent reversibility in the phase transition (*SI Appendix*, Fig. S6*A*). An LCST behavior is expected for LLPS that is primarily driven by hydrophobic interactions. The amino acid sequence of Y145Stop contains polar sequences enriched in glycine, serine, glutamine, and asparagine, along with aromatic amino acids (tryptophan, tyrosine, and phenylalanine) and positively charged residues (lysine and arginine). The observed thermoresponsive characteristics possibly point toward the dual behavior of aromatic amino acids central to both LCST and UCST characteristics. These aromatic residues can participate in intermolecular π–π stacking and cation–π interactions to promote LLPS (63, 65). Our phase separation assays using free arginine showed that LLPS of Y145Stop is abolished at higher concentrations of arginine, presumably due to strong interactions of free arginine with the aromatic sidechains that can potentially compete with intermolecular cation–π interactions (*SI Appendix*, Fig. S6 *B* and *C*).

These results indicate the participation of aromatic residues in promoting phase separation of Y145Stop. Taken together, this set of studies highlight the presence of promiscuous interactions (44) within the condensed environment of liquid-like droplets. The electrostatic screening allows the key noncovalent forces to promote transient, multivalent, interchain interactions between highly flexible conformers driving the liquid phase condensation of Y145Stop. Next, we set out to investigate the effect of these promiscuous noncovalent interactions in driving the maturation and conformational sequestration of these highly dynamic liquid droplets into ordered solid-like aggregates.

Phase Separation of Y145Stop Promotes the Formation of Self-Templating Amyloid-Like Aggregates. In order to monitor the maturation of Y145Stop condensates, we monitored the aging morphology of liquid droplets under a confocal microscope (Fig. 5*A*). The liquid-like characteristics of these droplets were retained for ∼5 h, after which these droplets irreversibly transformed into gel-like or solid-like fibrous morphologies. We observed "sea urchin"-like structures that were previously observed for FUS aggregates formed via LLPS (56). These results indicate that the droplets might act as the centers for nucleation and growth of fibers (Fig. 5*A*). The solid-like nature of these aggregates was also confirmed using FRAP, which showed no detectable recovery (Fig. 5*B*). These aggregates formed via the aging of liquid-like condensates are thioflavin-T^{+} (ThT^{+}) indicating a transition into amyloid-like aggregates (*SI Appendix*, Fig. S7 *A* and *B*). Our vibrational Raman spectroscopic investigation showed a sharp amide I band at 1,675 cm^{-1} that is a hallmark of hydrogen-bonded cross-β architecture in amyloid fibrils (Fig. 5*C*) (60). The FWHM of amide I considerably narrowed down from liquid droplets (∼63 cm^{-1}) to aggregates (∼44 cm^{-1}), indicating a more ordered and less heterogeneous conformational state. The ratio of the tyrosine Fermi doublet (I_{850}/I_{830}) decreased considerably upon liquid-to-solid transition from droplets (∼2.7) to aggregates (∼2.0), suggesting a buried environment of Tyr residues with a lower propensity to form hydrogen bonds with water (*SI Appendix*, Fig. S3). Additionally, the polarity around Trp also exhibited a small decrease as evident by a slight blue shift of the band around 880 cm^{-1}, indicating a lower hydrogen bonding ability of N-H of the indole ring with water within the aggregates. Also, this LLPS-mediated liquid-to-solid transition is characterized by the time-dependent evolution of intrinsic blue fluorescence (Fig. 5*D*) that arises due to the intermolecular charge-transfer and

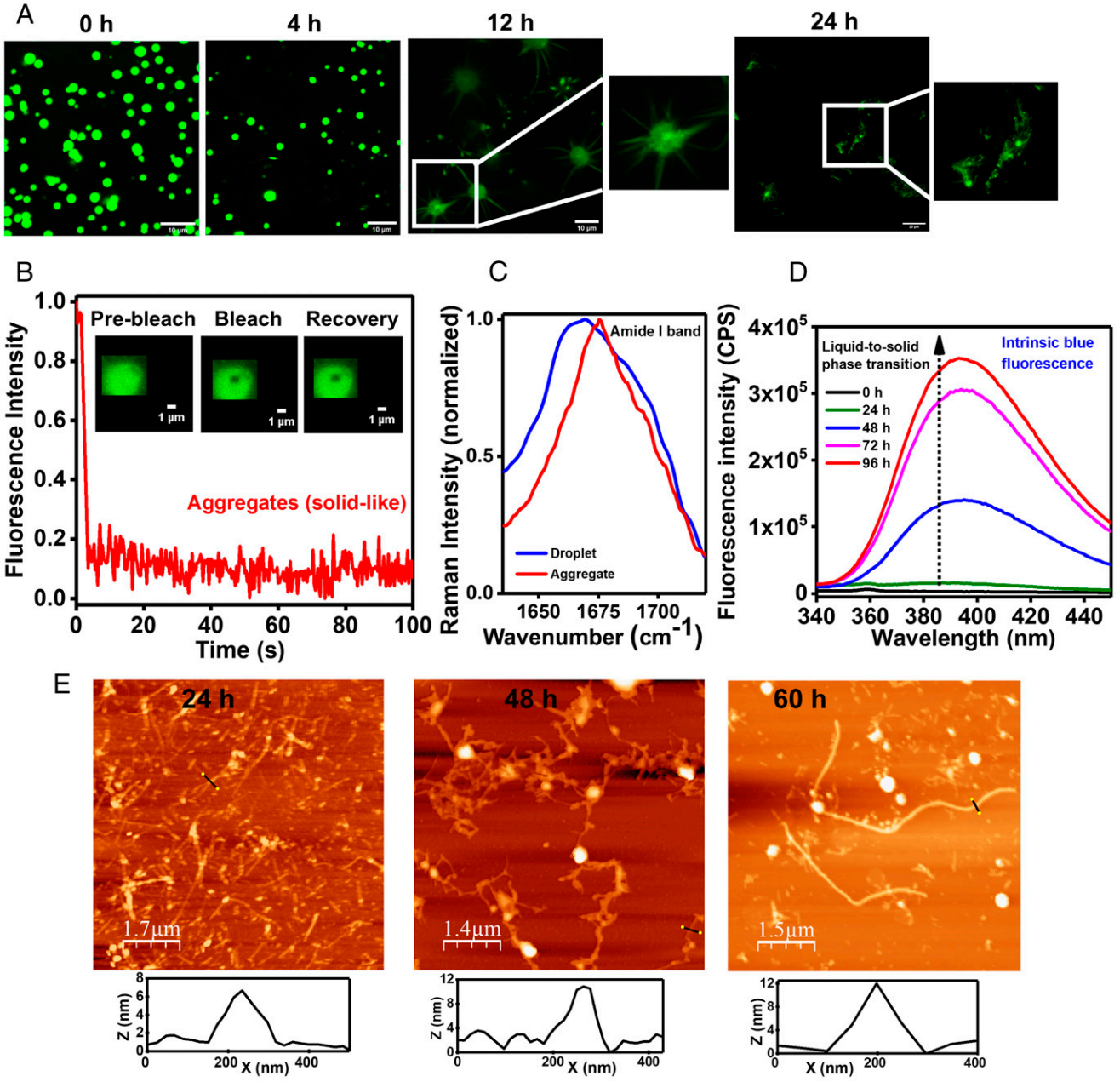

Fig. 5. Liquid-to-solid phase transition of Y145Stop. (*A*) Confocal images of fluorescently labeled Y145Stop showing morphological transitions as a function of time (for 12 h and 24 h images, 2× magnified regions are also shown). (*B*) FRAP kinetics of solid-like aggregates showing no recovery (fluorescence images during FRAP measurements are shown in the *Inset*). (*C*) Amide I vibrational Raman band showing a narrow peak at 1,675 cm^{-1}, indicating an amyloid-like cross-β architecture. (*D*) Time-evolution of the intrinsic blue fluorescence during maturation. (*E*) Time-dependent AFM images of aggregates formed via LLPS showing the presence of typical amyloid fibrils, with heights ranging from 8 to 12 nm.

electron delocalization via extensively hydrogen-bonded amide backbones within the phase-separated assemblies (66). Atomic force microscopy (AFM) imaging revealed a fibrillar nanoscale morphology along with some amorphous aggregates (Fig. 5*E*). Such amyloid fibrils with a height of ∼10 nm were also observed upon the phase transition and aging in the presence of RNA at a much lower protein concentration (*SI Appendix*, Fig. S7*C*). Together, these results suggest that during maturation, dynamic contacts within the condensates gradually change into more persistent interactions associated with a decrease in the conformational heterogeneity and a drop in the chain entropy ensuing in the sequestration of Y145Stop into a highly ordered amyloid-like architecture.

We next examined if the liquid droplets of full-length PrP are capable of converting into amyloid-like species under the same condition. These full-length PrP droplets upon aging did not exhibit an increase in the ThT fluorescence and remained ThT^{-}, indicating the C-terminal folded domain abolishes the liquid-to-solid maturation propensity (*SI Appendix*, Fig. S7*D*). This observation hints at a potentially protective role of the C-terminal globular domain in the absence of which the liquid droplets undergo an aberrant phase transition into amyloid-like aggregates. We next asked whether aggregates formed via phase separation of Y145Stop can exhibit a self-templating autocatalytic behavior that is a key characteristic of prion-like mechanisms.

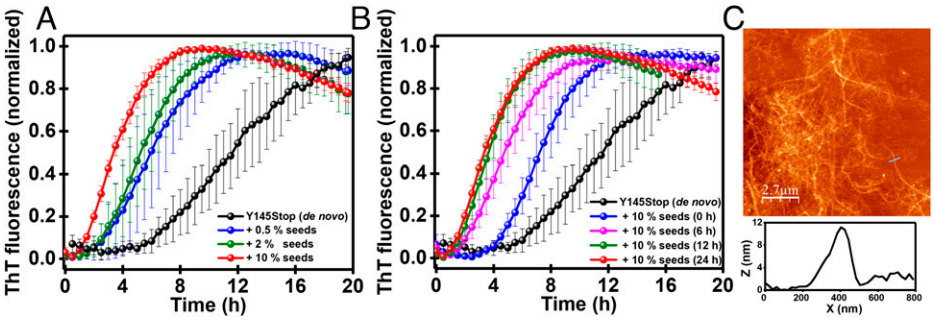

Fig. 6. Seeding behavior of aggregates formed via LLPS. (*A*) The shortening of the lag phase of de novo aggregation of Y145Stop (100 μM) by the addition of increasing amounts of amyloid seeds obtained from phase separation of Y145Stop. (*B*) The seeding efficiency monitored as a function of aging of phase-separated Y145Stop indicating the most effective seeding after phase maturation. (*C*) The AFM image of Y145Stop fibrils with the height profiles obtained after seeded assembly.

Next, in order to test if LLPS-mediated Y145Stop aggregates can exhibit a typical autocatalytic feature, we first carried out a de novo aggregation reaction with Y145Stop that is known to proceed via a typical nucleation-dependent polymerization mechanism (32). The de novo aggregation kinetics exhibited a lag time of ∼6 h. We then carried out these kinetic experiments in the presence of increasing amounts of preformed seeds obtained from the salt-induced LLPS-mediated phase transition and aging for 24 h. Upon addition of these seeds (0.5 to 10%), the lag phase shortened in a dose-dependent manner (Fig. 6*A*). By using 10% seeds in the reaction mixture, we were able to nearly bypass the lag phase ensuing quasi-pseudo first-order kinetics. After establishing that the aggregates formed via phase separation are capable of recruiting and inducing a self-perpetuating conformational conversion, we asked which key species during liquid-to-solid maturation exhibit the most potent self-templating characteristics. In order to answer this question, we performed aggregation assays using the preformed seeds generated by the phase separation process followed by different aging times. Liquid droplets formed immediately upon LLPS exhibited much weaker seeding ability compared to the aged samples that were prepared by maturation into β-rich aggregates via liquid-to-solid transitions (Fig. 6*B*). This observation suggests that amyloid conformers formed via the disorder-to-order phase transition are the key species in the autocatalytic conversion. The aggregation reaction seeded with aged solid-like species yielded typical amyloid fibrils reminiscent of nanoscale morphologies identical to fibrils formed via an unseeded de novo aggregation process (Fig. 6*C*). Together these findings reveal that aberrant phase transitions of Y145Stop can produce self-replicating amyloid species recapitulating the bona fide prion-like behavior.

Discussion

In this work, we showed that the intrinsically disordered Y145Stop containing oligopeptide repeats having a yeast prion-like domain and a low sequence complexity undergoes an instantaneous phase separation at near-neutral pH, concordant with the bioinformatic predictions. These phase-separated condensates, formed immediately after inducing LLPS, exhibit liquid-like characteristics having a highly mobile internal organization. The electrostatic screening of this highly positively charged N-terminal fragment at a higher salt concentration allowed the polypeptide chains to interact via weak and transient intermolecular contacts driving a reversible, thermo-responsive phase transition. Hydrophobic effects, along with other noncovalent interactions, serve as the physical cross-links essential for phase transitions. Single-droplet Raman measurements revealed that conformational disorder and structural heterogeneity are retained within the liquid-like droplets. Phase separation is further promoted by the addition of a molecular crowding agent at much lower protein and salt concentrations, mimicking the cytosolic milieu. Upon aging, liquid-like droplets gradually transform into irreversible, solid-like, highly ordered fibrillar aggregates that exhibit amyloid-like characteristics. These amyloids formed via phase separation of Y145Stop display the self-templating autocatalytic behavior that is a key characteristic of the prion-like propagation mechanism. Taken together, our results showcase the crucial role of the Y145Stop variant comprising the N-terminal IDR in driving aberrant phase transitions.

In contrast to Y145Stop, full-length PrP containing both N-terminal IDR and C-terminal globular domains, has a much lower propensity to phase-separate under the physiological condition in the presence of NaCl. Additionally, these liquid droplets of full-length PrP do not convert into typical amyloids, even upon prolonged incubation corroborating a previous finding (47). Our experimental observations are in line with the bioinformatic prediction indicating that the presence of the C-terminal folded domain can potentially offer protection from phase transitions. It is also pertinent here to highlight the key differences between the aggregation pathways of full-length PrP and the truncated variant, 145Stop. Full-length PrP containing the C-terminal GPI-anchor signal gets translocated to the membrane surface minimizing its duration in the cellular milieu. Thus, for the pathological conversion of full-length PrP involved in CJD, FFI, and so forth, the conventional protein misfolding event might be a prerequisite (26). This misfolding event is triggered by the destabilization due to mutations or partial unfolding of the C-terminal globular domain. In fact, a majority of CJD- and FFI-associated mutations are located near or in the C-terminal globular domain of PrP. In contrast, Y145Stop that is a cytoplasmic N-terminal IDR fragment devoid of the GPI-anchor can attain the self-seeding amyloid state via the (noncanonical) spontaneous phase-transition pathway without the stringent requirement for the protein misfolding step. This LLPS-mediated pathological conversion of Y145Stop can potentially provide a mechanistic underpinning of unusual variants of prion disease involving familial CAA and GSS syndrome.

Our findings reveal that RNA modulates the phase behavior of Y145Stop that contains putative RNA binding sites. Low RNA/protein ratios promote phase separation at a much lower Y145Stop concentration (∼5 μM) under the near-physiological condition (pH 7.5, 150 mM NaCl). RNA, being a polyanion, has a more pronounced influence in the electrostatic neutralization of highly positively charged IDR than the electrostatic screening by salt ions. Therefore, RNA binding allows the chains to interact via a multitude of noncovalent interactions, resulting in a complex coacervation. At low RNA/protein ratios, the RNA-induced droplets are more gel-like, less dynamic, and

rapidly transform into solid-like aggregates lacking internal fluidity. In contrast, at higher RNA/protein ratios, the phase separation ability of Y145Stop is abolished. These observations suggest that the RNA-protein stoichiometry is critical in the RNA-dependent phase transition of Y145Stop. Such modulation of physicochemical properties of condensates may indicate the context-dependent rewiring of interaction networks in the cellular milieu (67). The truncated Y145Stop variant is normally degraded by the proteasomal machinery or acted upon by the molecular chaperones. However, an impairment in the protein quality control allows this variant to accumulate in the endoplasmic reticulum, Golgi, and nucleus. Y145Stop overexpressed in cells treated with proteasome inhibitors has been shown to accumulate in the nucleus (35, 68). Its presence in the nucleus is analogous to the aggregates found in diseases with polyglutamine repeats expansion. The presence of Y145Stop aggregates in the nucleus has been ascribed to a cryptic nuclear localization signal (36), which is otherwise masked in full-length PrP that gets efficiently trafficked and translocated to the membrane surface. In addition, the cytoplasmic prion protein has been previously associated with the formation of ribonucleoprotein granules (51). Therefore, our findings also highlight a broader role of RNA in regulating the aberrant phase transition and amyloid formation of Y145Stop that is associated with CAA and GSS-like phenotypes.

In summary, our study unveils an intriguing interplay of molecular determinants that promote and regulate the phase transition and maturation into ordered self-templating amyloids from a pathological truncation variant of the prion protein. The phase separation propensity of the N-terminal IDR may potentially be important for clustering of the membrane-anchored cellular PrP. We would like to note that a putative function of PrP, such as copper homeostasis in the brain, involves the binding of Cu^{2+} with the oligopeptide repeats located at the N-terminal IDR (69, 70). Additionally, other proposed functions involving the maintenance of synaptic plasticity, suppressing apoptosis, and resistance to oxidative stress are also located at the N-terminal domain (69, 70). Even though the prion functions are mainly localized at the N-terminal segment, the C-terminal folded domain remains highly conserved during the vertebrate evolution (32). We, therefore, speculate that the C-terminal globular domain may potentially have a protective role in maintaining the solubility of the functional N-terminal domain preventing its aberrant phase transitions. The elimination of the C-terminal domain via 145 stop codon mutation not only converts a GPI-anchored protein into a cytoplasmic Y145Stop fragment, allowing it to undergo spontaneous intracellular phase transitions, but also exposes a key amyloidogenic determinant (residues 138 to 141) (32) that is otherwise masked in the loop region of full-length PrP. Our results underscore the crucial role of phase-separated droplets as the reaction crucibles for efficient nucleation and effective sequestration into self-perpetuating amyloid conformers. Additionally, our findings lend support to an emerging perspective, highlighting the importance of conformational heterogeneity, disordered interactions, and variable organization within the condensates in modulating the context-dependent interaction network responsive to the cellular environment, as well as in controlling the critical balance between droplet and amyloid states (2, 67). The interplay of these critical molecular events can have broad implications in biological phase transitions associated with physiology and disease.

Materials and Methods

Detailed materials and methods are included in *SI Appendix*. The human Y145Stop construct was created using the human PrP (23 to 231) plasmid. All mutations including single-Cys (Cys-31), A→G, and A→V mutants were created using a QuikChange site-directed mutagenesis kit (Stratagene). Cleavable N-terminal His-tagged recombinant proteins were expressed using *Escherichia coli* strain BL21(DE3) pLysS and His-tag was removed using thrombin. Phase separation assays were performed using turbidity measurements and confocal microscopy. FRAP experiments were performed using 1% Alexa Fluor488-C5-maleimide–labeled protein on a Zeiss LSM 980 attached with an Elyra 7 superresolution microscope. All the fluorescence experiments were performed on a FluoroMax-4 spectrofluorometer (Horiba Scientific) using a 1-mm pathlength quartz cuvette. Amyloid formation kinetics were performed using NUNC 96-well plate on a POLARstar Omega Plate Reader Spectrophotometer (BMG Labtech). Vibrational Raman spectroscopic studies were performed on an inVia laser Raman microscope (Renishaw) using a 100× objective lens (Nikon) and a 785-nm near infrared laser. AFM images were acquired using an Innova atomic force microscope (Bruker) operating in tapping mode.

Data Availability. All study data are included in the article and supporting information.

ACKNOWLEDGMENTS. We thank Prof. Witold Surewicz (Case Western Reserve University) for the kind gift of the DNA plasmid of full-length prion protein; Dr. Mahak Sharma (Indian Institute of Science Education and Research [IISER] Mohali) for confocal microscopy; Ms. Pallavi Joshi for preliminary studies; Dr. Shravan Mishra (IISER Mohali) for providing us yeast total RNA; Dr. Mily Bhattacharya (Thapar Institute), Dr. Priyanka Dogra (St. Jude Children's Research Hospital), Dr. Anupa Majumdar (Max Planck Institute of Molecular Cell Biology and Genetics), and the members of the S.M. laboratory for critically reading this manuscript; and the anonymous reviewers for their insightful comments and valuable suggestions. This study was funded in part by the IISER Mohali, Department of Science and Technology (Nano-Mission grant to S.M. and FIST grant); Department of Biotechnology (fellowship to A. Agarwal); Council of Scientific and Industrial Research (fellowship to S.K.R.); and the Ministry of Education, Government of India (Centre of Excellence grant to S.M.).

1. S. Alberti, A. A. Hyman, Biomolecular condensates at the nexus of cellular stress, protein aggregation disease and ageing. *Nat. Rev. Mol. Cell Biol.* **22**, 196–213 (2021).
2. M. Fuxreiter, M. Vendruscolo, Generic nature of the condensed states of proteins. *Nat. Cell Biol.* **23**, 587–594 (2021).
3. B. Portz, B. L. Lee, J. Shorter, FUS and TDP-43 phases in health and disease. *Trends Biochem. Sci.* **46**, 550–563 (2021).
4. M. Hardenberg, A. Horvath, V. Ambrus, M. Fuxreiter, M. Vendruscolo, Widespread occurrence of the droplet state of proteins in the human proteome. *Proc. Natl. Acad. Sci. U.S.A.* **117**, 33254–33262 (2020).
5. B. R. Sabari, A. Dall'Agnese, R. A. Young, Biomolecular condensates in the nucleus. *Trends Biochem. Sci.* **45**, 961–977 (2020).
6. F. Frottin *et al.*, The nucleolus functions as a phase-separated protein quality control compartment. *Science* **365**, 342–347 (2019).
7. S. Boeynaems *et al.*, Protein phase separation: A new phase in cell biology. *Trends Cell Biol.* **28**, 420–435 (2018).
8. S. F. Banani, H. O. Lee, A. A. Hyman, M. K. Rosen, Biomolecular condensates: Organizers of cellular biochemistry. *Nat. Rev. Mol. Cell Biol.* **18**, 285–298 (2017).
9. D. M. Mitrea, R. W. Kriwacki, Phase separation in biology; functional organization of a higher order. *Cell Commun. Signal.* **14**, 1 (2016).
10. A. A. Hyman, C. A. Weber, F. Jülicher, Liquid–liquid phase separation in biology. *Annu. Rev. Cell Dev. Biol.* **30**, 39–58 (2014).
11. J. A. Toretsky, P. E. Wright, Assemblages: Functional units formed by cellular phase separation. *J. Cell Biol.* **206**, 579–588 (2014).
12. J. M. Choi, A. S. Holehouse, R. V. Pappu, Physical principles underlying the complex biology of intracellular phase transitions. *Annu. Rev. Biophys.* **49**, 107–133 (2020).
13. E. W. Martin *et al.*, Valence and patterning of aromatic residues determine the phase behavior of prion-like domains. *Science* **367**, 694–699 (2020).
14. G. L. Dignon, R. B. Best, J. Mittal, Biomolecular phase separation: From molecular driving forces to macroscopic properties. *Annu. Rev. Phys. Chem.* **71**, 53–75 (2020).
15. S. Mukhopadhyay, The dynamism of intrinsically disordered proteins: Binding-induced folding, amyloid formation, and phase separation. *J. Phys. Chem. B* **124**, 11541–11560 (2020).
16. E. W. Martin, T. Mittag, Relationship of sequence and phase separation in protein low-complexity regions. *Biochemistry* **57**, 2478–2487 (2018).
17. K. M. Ruff, S. Roberts, A. Chilkoti, R. V. Pappu, Advances in understanding stimulus-responsive phase behavior of intrinsically disordered protein polymers. *J. Mol. Biol.* **430**, 4619–4635 (2018).
18. V. N. Uversky, Intrinsically disordered proteins in overcrowded milieu: Membraneless organelles, phase separation, and intrinsic disorder. *Curr. Opin. Struct. Biol.* **44**, 18–30 (2017).
19. C. P. Brangwynne, P. Tompa, R. V. Pappu, Polymer physics of intracellular phase transitions. *Nat. Phys.* **11**, 899–904 (2015).

20. B. Tsang, I. Pritišanac, S. W. Scherer, A. M. Moses, J. D. Forman-Kay, Phase separation as a missing mechanism for interpretation of disease mutations. *Cell* **183**, 1742–1756 (2020).
21. S. Ray *et al.*, α-Synuclein aggregation nucleates through liquid–liquid phase separation. *Nat. Chem.* **12**, 705–716 (2020).
22. S. Alberti, D. Dormann, Liquid–liquid phase separation in disease. *Annu. Rev. Genet.* **53**, 171–194 (2019).
23. S. Elbaum-Garfinkle, Matter over mind: Liquid phase separation and neurodegeneration. *J. Biol. Chem.* **294**, 7160–7168 (2019).
24. A. Aguzzi, M. Altmeyer, Phase separation: Linking cellular compartmentalization to disease. *Trends Cell Biol.* **26**, 547–558 (2016).
25. S. B. Prusiner, Prions. *Proc. Natl. Acad. Sci. U.S.A.* **95**, 13363–13383 (1998).
26. S. B. Prusiner, *Prion Biology* (Cold Spring Harbor Laboratory Press, 2017).
27. C. Scheckel, A. Aguzzi, Prions, prionoids and protein misfolding disorders. *Nat. Rev. Genet.* **19**, 405–418 (2018).
28. R. Zahn *et al.*, NMR solution structure of the human prion protein. *Proc. Natl. Acad. Sci. U.S.A.* **97**, 145–150 (2000).
29. J. Castilla, P. Saá, C. Hetz, C. Soto, In vitro generation of infectious scrapie prions. *Cell* **121**, 195–206 (2005).
30. N. R. Deleault, B. T. Harris, J. R. Rees, S. Supattapone, Formation of native prions from minimal components in vitro. *Proc. Natl. Acad. Sci. U.S.A.* **104**, 9741–9746 (2007).
31. F. Wang, X. Wang, C.-G. Yuan, J. Ma, Generating a prion with bacterially expressed recombinant prion protein. *Science* **327**, 1132–1135 (2010).
32. B. Kundu *et al.*, Nucleation-dependent conformational conversion of the Y145Stop variant of human prion protein: Structural clues for prion propagation. *Proc. Natl. Acad. Sci. U.S.A.* **100**, 12069–12074 (2003).
33. J. J. Helmus, K. Surewicz, P. S. Nadaud, W. K. Surewicz, C. P. Jaroniec, Molecular conformation and dynamics of the Y145Stop variant of human prion protein in amyloid fibrils. *Proc. Natl. Acad. Sci. U.S.A.* **105**, 6284–6289 (2008).
34. M. Zweckstetter, Conserved amyloid core structure of stop mutants of the human prion protein. *Prion* **7**, 193–197 (2013).
35. B. Ghetti *et al.*, Vascular variant of prion protein cerebral amyloidosis with tau-positive neurofibrillary tangles: The phenotype of the stop codon 145 mutation in PRNP. *Proc. Natl. Acad. Sci. U.S.A.* **93**, 744–748 (1996).
36. G. Zanusso *et al.*, Proteasomal degradation and N-terminal protease resistance of the codon 145 mutant prion protein. *J. Biol. Chem.* **274**, 23396–23404 (1999).
37. B. Xue, R. L. Dunbrack, R. W. Williams, A. K. Dunker, V. N. Uversky, PONDR-FIT: A meta-predictor of intrinsically disordered amino acids. *Biochim. Biophys. Acta* **1804**, 996–1010 (2010).
38. B. Mészáros, G. Erdős, Z. Dosztányi, IUPred2A: Context-dependent prediction of protein disorder as a function of redox state and protein binding. *Nucleic Acids Res.* **46**, W329–W337 (2018).
39. A. K. Lancaster, A. Nutter-Upham, S. Lindquist, O. D. King, PLAAC: A web and command-line application to identify proteins with prion-like amino acid composition. *Bioinformatics* **30**, 2501–2502 (2014).
40. M. Miskei, A. Horvath, M. Vendruscolo, M. Fuxreiter, Sequence-based prediction of fuzzy protein interactions. *J. Mol. Biol.* **432**, 2289–2303 (2020).
41. B. Bolognesi *et al.*, A concentration-dependent liquid phase separation can cause toxicity upon increased protein expression. *Cell Rep.* **16**, 222–231 (2016).
42. N. M. Milkovic, T. Mittag, "Determination of protein phase diagrams by centrifugation" in *Intrinsically Disordered Proteins. Methods and Protocols*, B. B. Kragelund, K. Skriver, Eds. (Springer, 2020), pp. 685–702.
43. J. P. Brady *et al.*, Structural and hydrodynamic properties of an intrinsically disordered region of a germ cell-specific protein on phase separation. *Proc. Natl. Acad. Sci. U.S.A.* **114**, E8194–E8203 (2017).
44. A. C. Murthy *et al.*, Molecular interactions underlying liquid–liquid phase separation of the FUS low-complexity domain. *Nat. Struct. Mol. Biol.* **26**, 637–648 (2019).
45. M. A. Kostylev *et al.*, Liquid and hydrogel phases of PrPC linked to conformation shifts and triggered by Alzheimer's amyloid-β oligomers. *Mol. Cell* **72**, 426–443.e12 (2018).
46. C. O. Matos *et al.*, Liquid–liquid phase separation and fibrillation of the prion protein modulated by a high-affinity DNA aptamer. *FASEB J.* **34**, 365–385 (2020).
47. H. Tange *et al.*, Liquid-liquid phase separation of full-length prion protein initiates conformational conversion in vitro. *J. Biol. Chem.* **296**, 100367 (2021).
48. M. P. B. Gomes, Y. Cordeiro, J. L. Silva, The peculiar interaction between mammalian prion protein and RNA. *Prion* **2**, 64–66 (2008).
49. R. Lathe, J.-L. Darlix, Prion protein PrP nucleic acid binding and mobilization implicates retroelements as the replicative component of transmissible spongiform encephalopathy. *Arch. Virol.* **165**, 535–556 (2020).
50. C. Gabus *et al.*, The prion protein has RNA binding and chaperoning properties characteristic of nucleocapsid protein NCP7 of HIV-1. *J. Biol. Chem.* **276**, 19301–19309 (2001).
51. S. Beaudoin *et al.*, A large ribonucleoprotein particle induced by cytoplasmic PrP shares striking similarities with the chromatoid body, an RNA granule predicted to function in posttranscriptional gene regulation. *Biochim. Biophys. Acta* **1793**, 335–345 (2009).
52. M. Hofweber *et al.*, Phase separation of FUS is suppressed by its nuclear import receptor and arginine methylation. *Cell* **173**, 706–719.e13 (2018).
53. Y. Lin, D. S. Protter, M. K. Rosen, R. Parker, Formation and maturation of phase-separated liquid droplets by RNA-binding proteins. *Mol. Cell* **60**, 208–219 (2015).
54. S. Elbaum-Garfinkle *et al.*, The disordered P granule protein LAF-1 drives phase separation into droplets with tunable viscosity and dynamics. *Proc. Natl. Acad. Sci. U.S.A.* **112**, 7189–7194 (2015).
55. T. Ukmar-Godec *et al.*, Lysine/RNA-interactions drive and regulate biomolecular condensation. *Nat. Commun.* **10**, 2909 (2019).
56. A. Patel *et al.*, A liquid-to-solid phase transition of the ALS protein FUS accelerated by disease mutation. *Cell* **162**, 1066–1077 (2015).
57. S. Maharana *et al.*, RNA buffers the phase separation behavior of prion-like RNA binding proteins. *Science* **360**, 918–921 (2018).
58. T. Kaur *et al.*, Sequence-encoded and composition-dependent protein-RNA interactions control multiphasic condensate morphologies. *Nat. Commun.* **12**, 872 (2021).
59. R. Tuma, Raman spectroscopy of proteins: From peptides to large assemblies. *J. Raman Spectrosc.* **36**, 307–319 (2005).
60. M. Bhattacharya, N. Jain, P. Dogra, S. Samai, S. Mukhopadhyay, Nanoscopic amyloid pores formed via stepwise protein assembly. *J. Phys. Chem. Lett.* **4**, 480–485 (2013).
61. A. M. Smith, A. A. Lee, S. Perkin, The electrostatic screening length in concentrated electrolytes increases with concentration. *J. Phys. Chem. Lett.* **7**, 2157–2163 (2016).
62. S. Kroschwald, S. Maharana, A. Simon, Hexanediol: A chemical probe to investigate the material properties of membrane-less compartments. *Matters (Zur.)* **3**, e201702000010 (2017).
63. J. Wang *et al.*, A molecular grammar governing the driving forces for phase separation of prion-like RNA binding proteins. *Cell* **174**, 688–699.e16 (2018).
64. F. Garcia Quiroz *et al.*, Intrinsically disordered proteins access a range of hysteretic phase separation behaviors. *Sci. Adv.* **5**, eaax5177 (2019).
65. S. Qamar *et al.*, FUS phase separation is modulated by a molecular chaperone and methylation of arginine cation-π interactions. *Cell* **173**, 720–734.e15 (2018).
66. P. Dogra, A. Joshi, A. Majumdar, S. Mukhopadhyay, Intermolecular charge-transfer modulates liquid–liquid phase separation and liquid-to-solid maturation of an intrinsically disordered pH-responsive domain. *J. Am. Chem. Soc.* **141**, 20380–20389 (2019).
67. M. Miskei *et al.*, Fuzziness enables context dependence of protein interactions. *FEBS Lett.* **591**, 2682–2695 (2017).
68. H. Lorenz, O. Windl, H. A. Kretzschmar, Cellular phenotyping of secretory and nuclear prion proteins associated with inherited prion diseases. *J. Biol. Chem.* **277**, 8508–8516 (2002).
69. M.-A. Wulf, A. Senatore, A. Aguzzi, The biological function of the cellular prion protein: An update. *BMC Biol.* **15**, 34 (2017).
70. B. Wu *et al.*, The N-terminus of the prion protein is a toxic effector regulated by the C-terminus. *eLife* **6**, e23473 (2017).